APS physics

CHORUS

This is the accepted manuscript made available via CHORUS. The article has been published as:

Interfacial mixing in high-energy-density matter with a multiphysics kinetic model

Jeffrey R. Haack, Cory D. Hauck, and Michael S. Murillo

Phys. Rev. E **96**, 063310 — Published 21 December 2017

DOI: 10.1103/PhysRevE.96.063310

Interfacial mixing in high-energy-density matter with a multiphysics kinetic model

Jeffrey R. Haack
Computational Physics and Methods Group, Los Alamos National Laboratory, P.O. Box 1663, Los Alamos, NM 87545

Cory D. Hauck
Computational and Applied Mathematics Group, Oak Ridge National Laboratory, P.O. Box 2008, Oak Ridge, TN 37831 and Department of Mathematics, University of Tennessee, Knoxville, TN 37996

Michael S. Murillo
Department of Computational Mathematics, Science and Engineering, Michigan State University, East Lansing, Michigan 48824

(Dated: December 7, 2017)

We have extended a recently developed multispecies, multitemperature BGK model [Haack *et al.*, J. Stat. Phys., 168, (2017)] to include multiphysics capabilities that enable modeling of a wider range of physical conditions. In terms of geometry, we have extended from the spatially homogeneous setting to one spatial dimension. In terms of the physics, we have included an atomic ionization model, accurate collision physics across coupling regimes, self-consistent electric fields, and degeneracy in the electronic screening. We apply the model to a warm dense matter scenario in which the ablator-fuel interface of an inertial confinement fusion target is heated, similar to the recent molecular dynamics study in [Stanton *et al.*, submitted to PRX], but for larger length and time scales and for much higher temperatures. Relative to this study, the kinetic model greatly extends the temperature regime and the spatio-temporal scales over which we are able to model. In our numerical results we observe hydrogen from the ablator material jetting into the fuel during the early stages of the implosion and compare the relative size of various diffusion components (Fickean diffusion, electrodiffusion, and barodiffusion) that drive this process. We also examine kinetic effects, such as anisotropic distributions and velocity separation, in order to determine when this problem can be described with a hydrodynamic model.

I. INTRODUCTION

Inertial confinement fusion (ICF) targets consist of a quantity of deuterium-tritium fuel surrounded by a shell of relatively higher Z material that symmetrically compresses the fuel to densities that are high enough to enable thermonuclear fusion reactions [1, 2]. ICF experiments span a wide range of density and temperature scales, from cryogenic temperatures at pre-shot to temperatures on the order of several kiloelectronvolts during burn. Degradation of the predicted fusion yield in ICF implosions is generally attributed to mixing of the shell material with the fuel, where energy losses through bremsstrahlung inhibit the sustained reaction. Hydrodynamic instabilities have long been viewed as a primary cause of this mix [3]. However, it has been shown in exploding pusher ICF experiments that such instabilities are not enough to explain the mix seen experimentally [4–6]. Plasma physics phenomena have been suggested to explain this, including barodiffusion at the fuel-shell interface [7, 8], plasma ionic diffusion [4, 9, 10], and large self-generated electric fields [8, 11]. However, it is unclear what the relative importance of each of these terms is at the various stages of the implosion.

Mixing at the fuel-shell interface in ICF has been studied with a wide variety of numerical methods and models. Experiments are often simulated by radiation hydrodynamics codes that account for mixing through the use of subgrid turbulence models verified by neutral fluid experiments [12–15]. However, these codes fail to capture both plasma phenomena and so-called kinetic effects. By kinetic effects we mean deviations from equilibrium, which can take the form of asymmetric distribution functions. Furthermore, multicomponent flows introduce an additional source of nonequilibrium behavior, namely, deviation from the mixture equilibrium. Plasma phenomena includes self-consistent electric fields, a self consistent ionization model, and electron degeneracy in the screening.

In an attempt to capture the plasma phenomena, consistent hydrodynamic models have been derived [16–18] for regimes where a fully kinetic description is not needed. Fully kinetic simulations such as particle in cell (PIC) methods [9, 19, 20] and Landau-Fokker-Planck models [21, 22] can capture non-equilibrium effects, such as Knudsen layers, and can explicitly incorporate a self-consistent electric field. However, the validity of these methods rests on the assumptions of low density and high temperature (weak coupling), which may not be applicable at all stages of the experiment. Molecular dynamics (MD), which intrinsically captures atomic mixing, dynamic many-body screening, partial ionization, electric fields, and non-hydrodynamic features (e.g., non-equilibrium distributions) can be used to obtain high-fidelity transport coefficients [23, 24]. However, MD is too computationally expensive to reach the time and length scales of interest in a dynamically evolving system due to the high densities and temperatures involved.

To summarize, the ICF target interface problem requires a model that can capture the kinetic effects caused by potentially anisotropic distributions at the interface. Additionally, the model must account for changes in the ionization state, screening, and plasma coupling regimes caused by the increase in temperature as the target rapidly heats up. Finally, the model must provide results at the time and length scales relevant to this process.

We propose to use a multispecies Vlasov-Poisson-BGK (VBGK) kinetic model [25] in which the collision rates are derived from Boltzmann cross sections computed using an effective potential approach [26] that accounts for dynamic screening and has been verified through MD calculations in weak to moderately strong coupling regimes. This has advantages over other kinetic models, requiring far less computation than full Boltzmann and Lenard-Balescu approaches and avoiding the weak coupling assumptions made in the Fokker-Planck approximation, which is more applicable to the later stages of the ICF implosion near burn. We also include evolving atomic physics through the use of a multispecies Thomas-Fermi partial ionization model [27, 28].

The remainder of the paper is organized as follows. In Sec. II we present the multiphysics VBGK model. We recall the conservative entropic BGK operator and the associated hydrodynamic equations, discuss collision rates and their consequences on transport properties, present the partial ionization model, and present several classical and quantum treatments for the Poisson equation. In Sec. III we demonstrate the new method by modeling a one dimensional ICF interface problem. We conclude and discuss paths forward in Sec. IV.

II. THE MULTIPHYSICS KINETIC MODEL

In this section we describe the components of the multiphysics kinetic model. First, we recall the multispecies BGK operator derived in [25] and the associated hydrodynamic equations. Then we discuss the incorporation of the effective Boltzmann cross sections from [26] into the BGK collision rates. Next, we compare the transport coefficients for the VBGK equation with those of an equivalent Boltzmann equation in the hydrodynamic limit. We then give a description of the multispecies mean ionization model and wrap up with a discussion of models used to treat the Poisson equation.

The multispecies VBGK equation for a mixture of N_s ion species is given by

$$\frac{\partial f_i}{\partial t} + \mathbf{c}\cdot\nabla_{\mathbf{x}} f_i + \frac{Z_i e}{m_i}\mathbf{E}\cdot\nabla_{\mathbf{c}} f_i = \sum_{j=1}^{N_s} Q_{ij}^{BGK}[f_i, f_j], \quad (1)$$
$$i = 1, \ldots, N.$$

Here $f_i = f_i(\mathbf{x}, \mathbf{c}, t)$ is the distribution of species i particles, with respect to the measure $d\mathbf{x}d\mathbf{c}$, located at position $\mathbf{x}$ with microscopic velocity $\mathbf{c}$ at time t. The mean ionization state of species i is given by $Z_i = Z_i(\mathbf{x})$, and e is the elementary charge. The electric field $\mathbf{E}$ is the solution to the Poisson equation

$$-\frac{1}{4\pi}\nabla_x^2\phi = \sum_i Z_i e n_i - e n_e, \quad (2)$$

$$\mathbf{E} = -\nabla_{\mathbf{x}}\phi, \quad (3)$$

where $n_e = n_e(\mathbf{x}, t)$ is the electron number density, the form of which we will specify later.

Macroscopic variables are defined by moments of the distribution functions f_i. For each i, the number density n_i, mass density ρ_i, and bulk velocity $\mathbf{v}_i$ are given by:

$$n_i = \int f_i d\mathbf{c}, \quad \rho_i = m_i n_i, \quad \mathbf{v}_i = \frac{1}{\rho}\int m_i \mathbf{c} f_i d\mathbf{c}, \quad (4)$$

where m_i is the particle mass for species i. The total number density n, total mass density ρ, and mass-averaged, or mixture, velocity $\mathbf{v}$ are defined by the relations

$$n = \sum_i n_i, \quad \rho = \sum_i \rho_i, \quad \rho\mathbf{v} = \sum_i \rho_i \mathbf{v}_i. \quad (5)$$

The species temperature T_i and mixture temperature T are given in energy units and are defined via the relations

$$\frac{3}{2} n_i T_i = \int \frac{m_i}{2}(\mathbf{c} - \mathbf{v}_i)^2 f_i d\mathbf{c}, \quad (6)$$

$$\frac{3}{2} n T = \sum_i \int \frac{m_i}{2}(\mathbf{c} - \mathbf{v})^2 f_i d\mathbf{c}. \quad (7)$$

A. The multispecies BGK operator

The operators Q_{ij}^{BGK} in (1) are defined as

$$Q_{ij}^{BGK}[f_i, f_j] = \nu_{ij}(\mathcal{M}_{ij}[f_i, f_j] - f_i), \quad (8)$$

where $\nu_{ij} = \nu_{ij}(\mathbf{x})$ is the collision frequency for interactions between species i and j and the Maxwellians $\mathcal{M}_{ij}$ are given by

$$\mathcal{M}_{ij}[f_i, f_j] = n_i \left(\frac{m_i}{2\pi T_{ij}}\right)^{3/2} \exp\left(-\frac{m_i(\mathbf{c} - \mathbf{v}_{ij})^2}{2T_{ij}}\right). \quad (9)$$

The Maxwellians vary in space and time via the parameters $\mathbf{v}_{ij} = \mathbf{v}_{ij}(\mathbf{x}, t)$ and $T_{ij} = T_{ij}(\mathbf{x}, t)$ that depend on f_i and f_j and are defined so that (i) conservation of momentum and energy hold for each species pair and (ii) the BGK equation satisfies an analog of Boltzmann's $\mathcal{H}$ Theorem. These conditions lead to the following expressions [25]:

$$\mathbf{v}_{ij} = \frac{\rho_i \nu_{ij}\mathbf{v}_i + \rho_j \nu_{ji}\mathbf{v}_j}{\rho_i \nu_{ij} + \rho_j \nu_{ji}}, \quad (10)$$

$$T_{ij} = \frac{n_i \nu_{ij} T_i + n_j \nu_{ji} T_j}{n_i \nu_{ij} + n_j \nu_{ji}} + \frac{\rho_i \nu_{ij}(v_i^2 - v_{ij}^2) + \rho_j \nu_{ji}(v_j^2 - v_{ij}^2)}{3(n_i \nu_{ij} + n_j \nu_{ji})}. \quad (11)$$

B. The hydrodynamic equations

For reference, the Navier-Stokes equations that correspond to the VBGK equation in the fluid limit are given by [25]

$$\frac{\partial \rho_i}{\partial t} + \nabla \cdot (\rho_i \mathbf{v}) + \nabla \cdot (\rho_i \mathbf{V}_i) = 0 \tag{12a}$$

$$\frac{\partial \rho \mathbf{v}}{\partial t} + \nabla \cdot (\rho \mathbf{v}\mathbf{v}) + \nabla \cdot \mathsf{P} = \sum_i n_i Z_i e \mathbf{E} \tag{12b}$$

$$\frac{3}{2}\left(\frac{\partial nT}{\partial t} + \nabla \cdot (nT\mathbf{v})\right) + \nabla \cdot \mathbf{q} + \mathsf{P} : \nabla \mathbf{v} \tag{12c}$$

$$= \sum_i n_i Z_i e \mathbf{E} \cdot \mathbf{V}_i, \tag{12d}$$

where $\mathbf{v}$ is the mixture velocity defined in (5) and T is the mixture temperature defined in (7). The pressure tensor P is given by

$$\mathsf{P} = pT - \eta((\nabla \mathbf{v} + (\nabla \mathbf{v})^T) - 2/3(\nabla \cdot \mathbf{v})\mathsf{I}), \tag{13}$$

where $p = nT$ and η is the viscosity. The diffusion velocities $\mathbf{V}_i = \mathbf{V}_i$ are given by

$$\mathbf{V}_i = \sum_j D_{ij} \mathbf{d}_j, \tag{14}$$

where D_{ij} are the symmetric diffusion coefficients and the diffusion driving forces $\mathbf{d}_j$ are given by

$$\mathbf{d}_i = \nabla x_i + (x_i - y_i)\nabla \log p + \frac{\rho_i}{p}\left(\frac{Z_i e}{m_i} - \sum_j y_j \frac{Z_j e}{m_j}\right)\mathbf{E}. \tag{15}$$

Here $x_j = n_j/n$ is the atom fraction and $y_j = \rho_j/\rho$ is the mass fraction. We refer to the first term in (15) as the *Fickean* diffusion term, the second as the *barodiffusion* term, and the third as the *electrodiffusion* term. The heat flux $\mathbf{q}$ is given by

$$\mathbf{q} = -K\nabla T + \frac{5T}{2}\sum_i n_i \mathbf{V}_i. \tag{16}$$

where K is the thermal conductivity. The transport coefficients D_{ij}, η, and K can all be derived from an underlying molecular model.

C. Cross sections and transport coefficients

In this subsection , we use the effective potential cross sections from [26] to define the collision rates ν_{ij} in (8). At the molecular level, binary interactions between charged particles are screened by what is an inherently many-body process. Screening is introduced into the binary collision framework of the Boltzmann operator through the use of effective potentials that are then used to generate cross sections that can be used in the Boltzmann description. Unlike the bare Coulomb potential, for which an exact but divergent analytic formula can be derived [29], these cross sections must be evaluated numerically.

In [26], numerical fits to the formulas for the momentum transfer cross section $\sigma_{ij}^{(1)}$ and the Chapman-Enskog collision integrals $\Omega_{ij}^{(lm)}$ are given for dense plasmas [30]. These formulas are used to define transport coefficients in the hydrodynamic limit and also arise in calculation of momentum and temperature exchange rates. While the Boltzmann description was originally derived in the context of dilute gases, these cross sections extend the validity of the Boltzmann framework to dense plasmas and have been verified using molecular dynamics over a wide range of plasma conditions. For more details, see [26].

We define the collision rates used in the BGK operator (8) by constraining them to match either the momentum relaxation rate ν_{ij}^M or the temperature relaxation rate ν_{ij}^T of the Boltzmann collision operator [25]. These rates are given by

$$\nu_{ij}^M = \frac{1}{\rho_i}\frac{128\pi^2 n_i n_j (m_i m_j)^{3/2}(Z_i Z_j e^2)^2}{3(2\pi)^{3/2}\mu_{ij}(m_j T_i + m_i T_j)^{3/2}}\mathcal{K}_{11}(\gamma_{ij}), \tag{17}$$

$$\nu_{ij}^T = \frac{1}{n_i}\frac{256\pi^2 n_i n_j (m_i m_j)^{1/2}(Z_i Z_j e^2)^2}{3(2\pi)^{3/2}(m_i T_j + m_j T_i)^{3/2}}\mathcal{K}_{11}(\gamma_{ij}), \tag{18}$$

$$\gamma_{ij} = \frac{2Z_i Z_j e^2(m_i + m_j)}{2(m_i T_j + m_j T_i)\lambda_{\text{eff}}}, \tag{19}$$

for the momentum and temperature relaxation rates, respectively. Formulas for the nondimensional collision integrals $\mathcal{K}_{11}$ [31] and the effective screening length λ_{eff} are given in [26]. In the remainder of the paper, we refer to the BGK operator using the momentum relaxation collision rate (17) as BGK-EM, and the one using the temperature relaxation collision rate (18) as BGK-ET.

To get an idea of how the BGK approximation affects the hydrodynamic limit, we make comparisons between the transport coefficients derived in [25], corresponding to the multispecies BGK model, and those derived by Stanton and Murillo (SM) in [26] for the Boltzmann equation using effective potential cross sections.

A priori we expect the BGK diffusion coefficient to have a similar value to the Boltzmann diffusion coefficient because they use the same cross sectional data, i.e. $\Omega_{ij}^{(11)}$. Indeed, the formula for the diffusion coefficient in [26] is

$$D_{ij} = \frac{3T}{16 n \mu_{ij}\Omega_{ij}^{(11)}} = \frac{3T^{5/2}}{16\sqrt{2\pi\mu_{ij}}n Z_i^2 Z_j^2 e^4 \mathcal{K}_{11}(g)}, \tag{20}$$

where $\mathcal{K}_{11}$ is a non-dimensional fitting function related to the the Chapman-Enskog collision integral $\Omega_{ij}^{(11)}$ by

$$\Omega_{ij}^{(nm)} = \sqrt{\frac{2\pi}{\mu_{ij}}}\frac{(Z_i Z_j e^2)^2}{T^{3/2}}\mathcal{K}_{nm}. \tag{21}$$

This same function is used in the definition of the collision rates for the BGK-EM and BGK-ET models (see (17) and (18)). However in the Boltzmann description, transport coefficients such as the viscosity η and thermal conductivity K use the Chapman-Enskog collision integrals, $\Omega_{ii}^{(22)}$. The mixture viscosity η and thermal conductivity K formulas are built using the individual species viscosities η_i and thermal conductivites K_i:

$$\eta_i = \frac{5T}{8\Omega_{ii}^{(22)}} = \frac{5\sqrt{m_i}T^{5/2}}{16\sqrt{\pi}Z_i^4 e^4 \mathcal{K}_{22}(g)}, \tag{22}$$

$$K_i = \frac{75T}{32 m_i \Omega_{ii}^{(22)}} = \frac{75T^{5/2}}{64\sqrt{\pi m_i}Z_i^4 e^4 \mathcal{K}_{22}(g)}. \tag{23}$$

For more details on how these are combined to make the mixture viscosity and thermal conductivity, see [26] and [30]. Note that the values of $\Omega_{ii}^{(22)}$ are not accounted for when defining the collision rates in the BGK model.

It is convenient in what follows to investigate the behavior of transport coefficients in terms of two dimensionless parameters [26]. The first parameter is the Coulomb coupling between species i and j, which is a measure of the ratio of average potential to kinetic energy. It is given by $\Gamma_{ij} = Z_i Z_j e^2/a_{tot}T$, where the total ion-sphere radius $a_{tot} = (3/4\pi n)^{1/3}$ is used to estimate the spacing between the particles. The second parameter, which measures electronic screening, is given by $\kappa = a_{tot}/\lambda_e$. We plot the nondimensional transport coefficients

$$D_{12}^* = \frac{D_{12}}{\omega_p a_{tot}^2} \quad \text{and} \quad \eta^* = \frac{\eta}{m_i n_i \omega_p a^2}, \tag{24}$$

where ω_p is the plasma frequency, versus these two parameters.

We first compare the interdiffusion coefficient of the SM and BGK models for a binary mixture of hydrogen and helium relevant to stellar interiors [32]. In this case there is no electron screening, and we assume a 50-50 mixture of fully ionized hydrogen and helium. In Fig. 1 we plot the nondimensionalized diffusion coefficient D_{12}^* versus the coupling parameter Γ_{12}. In this case, BGK-ET gives exactly the same result as the Boltzmann model, while the BGK-EM model under-predicts the diffusion coefficient with a relative error of 36%.

Next we compare the viscosity coefficient of the BGK and SM models for a single-species hydrogen plasma. Because the BGK collision rates in (17) and (18) do not take in to account the term $\Omega_{11}^{(22)}$ in the SM viscosity formula from (22), we expect some disagreement between the models. In Fig. 2, we compare η^* for varying Γ and with $\kappa = 1$. For same-species collisions the BGK-EM and BGK-ET collision rates are identical, so only one BGK plot is shown. In this case, the BGK model underpredicts the viscosity by 20-24% but follows the trend of the SM model and the MD, for low coupling parameters.

Finally we compare the thermal conductivity coefficient of the BGK model to the SM effective potentials

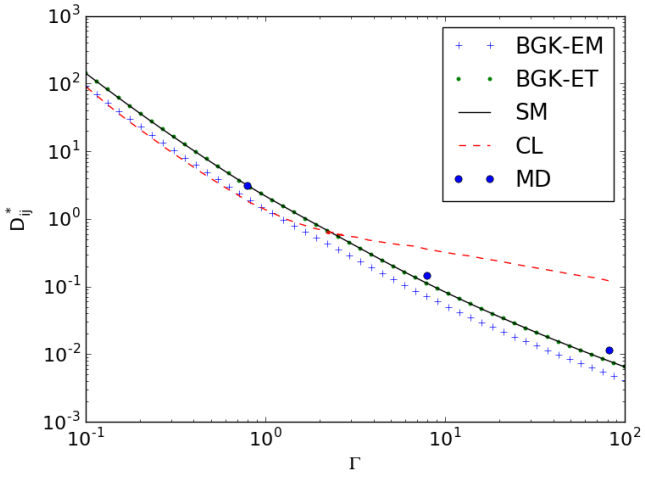

FIG. 1. **Interdiffusion coefficient.** Shown are the predictions of the nondimensionalized interdiffusion coefficients D_{ij}^* for a mixture of hydrogen and helium over a range of Γ. The BGK-ET model (small circles) coincides with the SM model (solid line), and the MD results (large circles), which is expected since the formulas are based on the same collision integral $\Omega_{ij}^{(11)}$. The BGK-EM model (plus symbols) predicts less diffusion than the SM model. However, it tracks the trend of the MD results into the moderately coupled regime, unlike the classical Coulomb logarithm theory (dashed line)

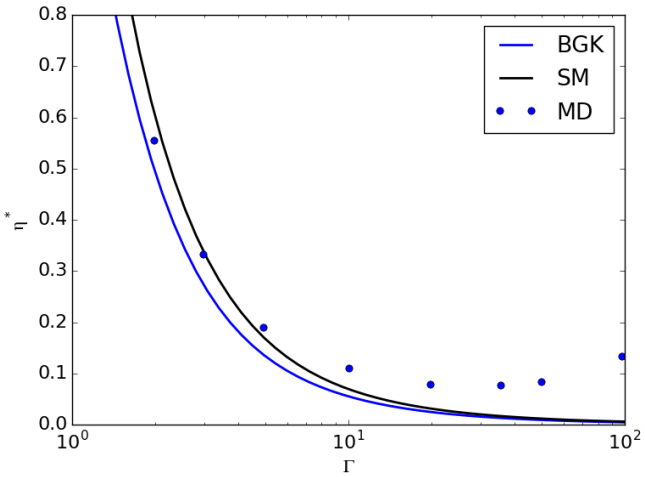

FIG. 2. **Viscosity coefficient.** Shown above are predictions of the nondimensionalized viscosity η for a hydrogen plasma over a range of Γ. The BGK model (lower, blue line) again predicts a smaller transport coefficient, but follows the trend of the SM model (upper, black line). (In the single species case, the BGK-EM and BGK-ET versions are the same.) Both the BGK and SM models fail to capture the turning point of the viscosity for stronger coupling that is seen in the MD results (large circles).

model for the same single species hydrogen plasma. As in the viscosity case, we do not expect exact agreement since the BGK model does not have the information from $\Omega_{11}^{(22)}$ built into it. The BGK model underpredicts the thermal conductivity by 28-29%.

The differences in transport coefficient are a natural consequence of how the BGK operator is constructed, as there are only so many constraints that one can use in defining the model [25]. One possibility for improving the BGK coefficients is to use an ellipsoidal, or ES-BGK, model [33], where the spherically Maxwellians in (8) are replaced by possibly anisotropic gaussians, which adds additional degrees of freedom to the target distributions. This topic will be explored in future work.

D. Mean Ionization State in Mixtures

One of the simplest models for determining the mean ionization state Z_i of a single species plasma is the Thomas-Fermi model. In this model, $Z_i = Z_i(n_i, T_e)$ is expressed as a function of the number density n_i and electron temperature T_e by calculating the atomic structure of a charge-neutral spherical shell. The number density affects this calculation by adjusting the size of the bounding shell, and the ionization state is determined in terms of the electron density on the shell. To further simplify this calculation, a fit to the Thomas-Fermi model for the ionization state was given in [34]. Despite the relative simplicity of this model compared to more complete atomic structure models, it is nevertheless accurate over a wide range of parameters; see [35].

Here we build on this single species representation to derive an analogue in the multispecies setting. For each species, we determine the partial ionization using the single species Thomas-Fermi model, with two additional considerations. First, the ion sphere radius must take into account the number density of each species in order to more correctly capture pressure ionization effects. In addition, we require that the free electron density is uniform beyond the ion spheres for each species. Thus we require

$$\frac{Z_i}{V_i} = \frac{Z_j}{V_j}, \qquad \forall i, j, \tag{25}$$

where V_i is the volume of the ion spheres associated with species i and $Z_i = Z_i(n_1, ..., n_N, T_e)$. To complete the system, we add the volumetric constraint

$$\sum_j n_j V_j = 1. \tag{26}$$

The nonlinear system (25)-(26) is solved with an iterative method. For more details and the specific algorithm used to solve (25), see [27].

E. Electronic Charge Density Models

The models considered in the present work do not explicitly model electrons as a dynamically evolving species. Rather, they are treated in the zero mass limit where they implicitly follow the ion dynamics, forming screening clouds that modify the bare ion-ion interactions. There are many modeling choices that can be made for the electronic densities. In an effort to understand the model's sensitivity to these choices more deeply, we construct four separate treatments of the electronic density: (1) the classical Poisson-Boltzmann model (PB), (2) the quantum Poisson-Thomas-Fermi model (PTF), (3) the (linear) Debye-Hückel model (DH), and (4) a linearized Thomas-Fermi model (LTF). In general the PTF model is expected to have the highest fidelity because of its treatment of partial degeneracy and the fact that the other models rely on linearized approximations. In the classical limit it recovers the PB model, and when a linearization of that is valid, it recovers the DH model. Because it is also possible that the screening is linear, but with partially degenerate electrons, we include the LTF. It is also possible to describe correlations beyond these models using, for example, integral equation approaches such as the hypernetted chain approximation [36]; for example, the V-BGK approach could be modified to include the radial distribution function [37] in the electric field term [38], but we leave these extensions to future work and explore just these four models.

1. Poisson-Boltzmann model (PB)

In the thermal equilibrium, classical, mean-field limit we obtain the (non-linear) electronic number density

$$n_e = n_{e0}\exp(e\phi/T_e), \tag{27}$$

where $T_e = T_e(\mathbf{x}, t)$ is the electron temperature and n_{e0} is a parameter that ensures the conservation of electron number. In this paper we approximate it as the average electron number density of the entire system. By we inserting the formula in (27) into the Poisson equation (2), we obtain the "Poisson-Boltzmann" equation [39]

$$-\nabla_{\mathbf{x}}^2\phi = 4\pi e\left(\sum_i Z_i n_i - n_{e0}\exp(e\phi/T_e)\right). \tag{28}$$

When coupled with the equations of motion for the ions, (28) induces screened ionic interactions in a classical, non-linear fashion.

2. Debye Hückel model (DH)

To understand the role of non-linearity in electronic screening, we also examine the linear limit of (27), which

can be significantly faster to compute. In this limit, the electron density (27) has the expansion

$$n_e \approx n_{e0}(1 + e\phi/T_e) \tag{29}$$

that, when subsituted into (28), results in a linear Helmholtz equation

$$-\nabla_{\mathbf{x}}^2\phi + \frac{4\pi n_{e0}e^2}{T_e}\phi = 4\pi e\left(\sum_i Z_i n_i - n_{e0}\right). \tag{30}$$

This equation recovers the classical (i.e., Debye-Hückel) electron screening length $\lambda_e^{-2} = 4\pi n_{e0}e^2/T_e$.

3. Poisson-Thomas-Fermi model (PTF)

Many dense plasmas are created from rapidly heated solids and are therefore partially degenerate at least for times shortly after ionization. Degeneracy is most easily modeled using the finite-T_e Thomas-Fermi approach for which the electronic density has the form

$$n_e = \frac{2(2\pi m_e T_e)^{3/2}}{(2\pi\hbar)^3}\mathcal{F}_{1/2}((e\phi + \mu)/T_e). \tag{31}$$

The chemical potential μ, which we will define below, enforces the mean number of electrons (usually by charge conservation), and $\mathcal{F}_{1/2}$ is a Fermi integral, defined as [40]

$$\mathcal{F}_j(x) = \int_0^\infty \frac{t^j}{e^{t-x}+1}dt. \tag{32}$$

By inserting the expression in (31) for n_e into (2), we obtain the nonlinear Poisson-Thomas-Fermi equation

$$-\nabla_{\mathbf{x}}^2\phi = 4\pi e\left(\sum_i Z_i n_i - \frac{2(2\pi m_e T_e)^{3/2}}{(2\pi\hbar)^3}\mathcal{F}_{1/2}((e\phi+\mu)/T_e)\right) \tag{33}$$

4. Linear Thomas-Fermi model (LTF)

The Poisson-Thomas-Fermi electron density (31) can be linearized as

$$n_e \approx \frac{2(2\pi m_e T_e)^{3/2}}{(2\pi\hbar)^3}\left(\mathcal{F}_{1/2}(\mu/T_e) + \mathcal{F}_{-1/2}(\mu/T_e)(e\phi/T_e)\right). \tag{34}$$

This formula, when substituted into (33), results in a linear Helmholtz equation

$$-\nabla_{\mathbf{x}}^2\phi + \frac{8\pi e^2(2\pi m_e T_e)^{3/2}\mathcal{F}_{-1/2}(\mu/T_e)}{T_e(2\pi\hbar)^3}\phi \tag{35}$$
$$= 4\pi e\left(\sum_i Z_i n_i - \frac{2(2\pi m_e T_e)^{3/2}}{(2\pi\hbar)^3}\mathcal{F}_{1/2}(\mu/T_e)\right),$$

that naturally recovers the Thomas-Fermi screening length

$$\lambda_{TF}^{-2} = \frac{8\pi e^2(2\pi m_e T_e)^{3/2}\mathcal{F}_{-1/2}(\beta\mu)}{T_e(2\pi\hbar)^3} \tag{36}$$

and is the arbitrary-dengeneracy generalization of the Debye-Hückel result (30).

The chemical potential μ enforces global charge conservation across the domain in the PTF and LTF models. Rather than using a global solve to find μ, we determine a local value μ_j in each computational cell of the numerical discretization by solving the nonlinear equation relating n_e and μ:

$$\sum_i Z_i(x_j)n_i(x_j) = n_e(x_j) = \frac{2(2\pi m_e T_e)^{3/2}}{(2\pi\hbar)^3}\mathcal{F}_{1/2}(\beta\mu_j). \tag{37}$$

The global value of μ used in (31) and (34) is taken to be the average of these μ_j. In numerical tests this approximation has resulted in a negligible charge loss, with a relative error of roughly 10^{-7}.

III. NUMERICAL RESULTS

In this section we present numerical results for a 1D-3V, ICF inspired interface scenario. ICF targets are often designed with an outer ablator shell that surrounds a dense deuterium-tritium fuel layer. The ablator contains non-fusion burning elements that are harmful to the thermonuclear burning of the fuel; worse, higher-Z elements can radiate energy away from the fuel region. Thus it is important to understand how ablator and fuel species mix at the interface as the target is heated.

Initially on the left side of the computational domain we have a CH shell material (a model for a plastic ablator) that is doped with a small amount of oxygen, and on the right side we have DT ice (see Table I for initial number densities). We consider two problems: one with a temperature range of 10-50 eV and the other a 100-300 eV range. In both cases, we focus on the evolution during the early stages of the implosion. The ion species are initialized as Maxwellians with zero bulk velocity and a specified temperature, and energy is put into the system through a specified electron temperature T_e that affects the electric field calculation and transfers energy to the ions through an additional collision term:

$$Q_{ei}^{\mathrm{BGK}} = \nu_{ei}(\mathcal{M}_{ei}(n_e, T_e) - f_i). \tag{38}$$

The electron number density n_e is given by $n_e = \sum_j Z_j n_j$, and the electron-ion collision rate ν_{ei} is calculated using a screened Coulomb cross section; the formula for ν_{ei} can be found in [25].

The VBGK equation (1) is solved numerically using a second-order Strang splitting of the Vlasov operator

$$f_i \mapsto -\mathbf{c}\cdot\nabla_{\mathbf{x}} f_i - \frac{Z_i e}{m_i}\mathbf{E}\cdot\nabla_{\mathbf{c}} f_i \tag{39}$$

and the BGK operator

$$f_i \mapsto \sum_j Q_{ij}^{BGK}. \tag{40}$$

The Vlasov equation is solved using a standard second-order finite volume method with the monotonized central difference limiter [41]. The Poisson equation to determine the electric field (see Section II E) is discretized to second-order and solved with Newton's method for the nonlinear models PB (28) and PTF (33), and a linear algebra solve for the linear models DH (30) and LTF (35). We use a second-order SSP Runge-Kutta method [42] for the time integration of each split step. For the 10-50 eV case, the physical domain width is two microns ($x \in [-1, 1]$), and the initial interface is located at the center ($x = 0$). We use periodic boundary conditions and compute to a final time of 10 ps. For the 100-300 eV case, we use a physical domain size of 50 microns ($x \in [-25, 25]$), again with the initial interface at $x = 0$, and compute to a final time of 50 ps.

The VBGK equation cannot simulate exactly the same test problem formulated for the molecular dynamics study in [27], which starts from a very low, nearly cryogenic temperature and ramps up to 50 eV. This is due to the expense of numerically representing the distribution functions across several orders of magnitude of temperature, as one would need a grid that both resolves the narrow peak of a cold distribution and is wide enough to capture the tails of a hot distribution. Some approaches exist for modifying velocity grids to account for this; see [43, 44] for an interpolation approach for the 1V and 2V single species BGK operator and [45] for a moment-based rescaling of velocity space in the context of the Landau-Fokker-Planck operator. This is an area that we intend to explore further in future work. In contrast to MD [27], the VBGK model can model much higher temperature plasmas for which MD is limited by timestep issues associated with hard collisions and the large number of interactions that must be considered, due to much weaker screening.

In the numerical examples that follow, we simulate systems with a smaller relative change in temperature (10-50eV, 100-300eV) that do not require excessive memory costs. For the 10-50 eV case, we also present simulations where the ion temperature is assumed to be instantly heated to the maximum electron temperature, similar to what was done in [27].

H	C	O	D	T
4.663×10^{22}	6.305×10^{22}	5.511×10^{20}	2.994×10^{22}	2.994×10^{22}

TABLE I. Initial number densities for the interface problem. Units are cm^{-3}.

A. Electric Field comparisons

We begin by comparing the four treatments of the Poisson equation given in Sec. II E. We use the initial number densities for the interface problem and initialize the ion temperature at 10 eV. The background electron temperature is fixed at 10 eV for the entirety of the run. In Fig. 3, we compare the nonlinear PB model with the nonlinear PTF model at four different times. The linear versions of these models, DH and LTF respectively, are not shown as they are very similar to the PB case. There is a strong electric field at the initial time for all of the models due to the discontinuity at the interface, and a significant electric field persists as the interface diffuses. The peaks in the figures correspond to the shell-gas interface and a wave in the gas that arises from compression. The PTF model shows a much stronger electric field than the others, while the PB and linear models mostly agree with one another. While all of the models show a significant electric field at later time, we use the PTF model in all future calculations as it should give the largest and most interesting possible electric field effects on the evolution of the macroscopic variables.

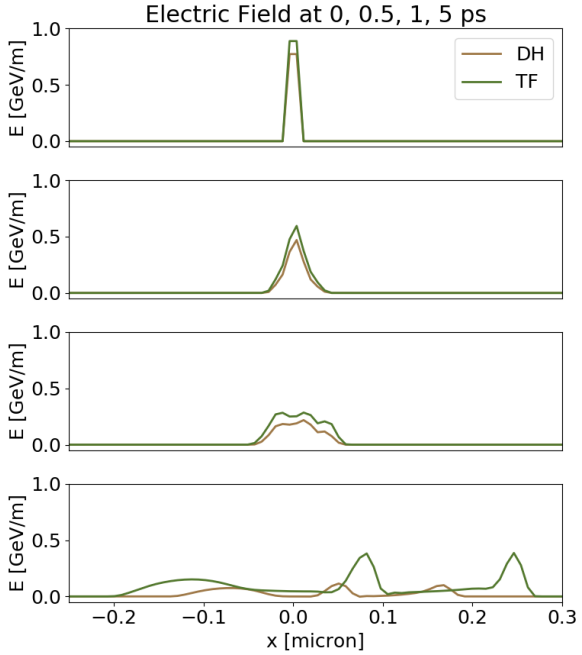

FIG. 3. **Electric field models.** A comparison of the electric field models is shown at 0 fs, 500 fs, 1 ps, and 5 ps for an instantly heated 10 eV interface. The spike in electric field due to the discontinuity at the initial time rapidly decreases but the field strength remains significant. The PTF model (green upper line) notably produces a much stronger electric field than the PB model (brown lower line). The DH and LTF solutions are excluded from the figure as they track very closely to the PB profile.

B. Interface at 10-50 eV

Next, we study the evolution of the interface in the range of 10 eV to 50 eV. The ion temperature is initialized at 10 eV, and the electron temperature is increased from 10 eV to 50 eV at a rate of 5 eV/ps. We use 256 points in space and a 40^3 velocity grid, which is sufficient to resolve the early and late time ion distribution functions, and we use the PTF model (33) to model the Poisson equation. For comparison, we also present the evolution of the interface where the ion temperatures are initialized at 50 eV and the electron temperature is fixed at 50 eV. This mimics the 'instant heating' of the MD study in [27].

In Fig. 4 we show the species density profiles at 500 fs and 10 ps. The hydrogen leads the carbon into the gas; the effect is especially strong in the instant heating case. At 500 fs, a shock appears to be forming in the DT gas, just to the right of the interface, as it is compressed by the moving shell material.

In Fig. 5 we show the species diffusion velocity profiles at 500 fs and 10 ps. There is a significant separation from the mixture velocity in the mixing layer. This indicates that the usual single-velocity hydrodynamic approximation may not apply here, as the Chapman-Enskog expansion used to derive the Navier Stokes equations (12d) requires that there are only small deviations from the mixture velocity $\mathbf{v}$.

C. Interface at 100-300 eV

Above 50 eV or so, MD is limited by timestep issues associated with hard collisions as well as the increasing computational cost caused by much weaker screening, as each particle interacts with increasingly more particles [27]. To demonstrate that the multispecies VBGK model can reach time, length, and temperature scales beyond those that MD is capable of, we consider the evolution of the interface in the range of 100 eV to 300 eV. The ion temperature is initialized at 100 eV, and the electron temperature is increased from 100 eV to 300 eV at a rate of 5 eV/ps. We use 128 points in space and a 40^3 velocity grid, which is sufficient to resolve the early and late time ion distribution functions, and we use the PTF model (33) for the Poisson equation. We extend the size of the physical domain to 50 microns, and simulate the interface dynamics to 50 ps.

In Fig. 6 we show the species density profiles at 5 ps and 50 ps. As before, the hydrogen leads the carbon into the gas, but the diffusion into the gas region is much more rapid at higher temperature. Related to this, we see a small but significant separation from the mixture velocity in the mixing layer. In Fig. 7 we show the evolution of the electric field at four different times. As in the lower temperature case, the electric field remains significant throughout the simulation. In Fig. 8 we show the evolution of the carbon and oxygen ionization states at four different times. There is a significant increase in ionization over this temperature range, which affects the collision rates and electric fields. At these temperatures, the hydrogenic species are effectively fully ionized for the duration of the simulation, so this information is excluded from the figure.

D. Nonequilibrium flow features

Next we examine nonequilibrium features of the distribution functions. To quantify non-equilibrium behavior, we calculate for each species the ratio of the normal and transverse temperature components T_x and T_y:

$$T_{i,x} = \frac{1}{n_i}\int \frac{m_i}{2}(c_x - v_{i,x})^2 f_i d\mathbf{c} \tag{41}$$

$$T_{i,y} = \frac{1}{n_i}\int \frac{m_i}{2}(c_y - v_{i,y})^2 f_i d\mathbf{c}, \tag{42}$$

where $v_{i,x}$ and $v_{i,y}$ are the x (normal) and y (transverse) components of the species bulk velocity [46]. Because we have already observed velocity separation between the species, we use the species velocities $\mathbf{v}_i$ rather than the mass-averaged mixture velocity $\mathbf{v}$ to probe the distribution functions. Deviations from a T_x/T_y ratio of one indicate a non-equilibrium distribution. In the left plot of Fig. 9, we show the temperature component ratio at 5 ps for this test case. There is some deviation in the leading edge of the diffusing interface, suggesting a small kinetic effect in this temperature range. For comparison, in the right plot of Fig. 9 we plot the same interface problem with a fixed background temperature of 20 keV, which is on the order of the highest designed temperature for ICF experiments. As expected there are larger deviations from equilibrium in this regime, verifying that this model does show kinetic effects in the regime where they are expected.

We also computed third order (heat flux) and fourth order moments of the distribution functions in the direction of the flow in order to determine whether the tails of the distribution function were non-Maxwellian. Namely,

$$\mathbf{q}_{i,x} = \int \frac{m_i}{2}(c_x - \mathbf{v}_{i,x})(\mathbf{c} - \mathbf{v}_i)^2 f_i d\mathbf{c} \tag{43}$$

$$\langle v^4 \rangle_{i,x} = \int (c_x - v_{i,x})^4 f_i d\mathbf{c}. \tag{44}$$

When compared to the exact solutions obtained from a Maxwellian distribution, the differences were negligible.

In order to get a sense of the impact of kinetic effects (or lack thereof) on the hydrodynamic variables, we compare these results with those of a hydrodynamic solution that is computed with a kinetic scheme [47]. This scheme is implemented with the same VBGK kinetic code, but is obtained by resetting each distribution function to its associated Maxwellian at each time step. The result is a multicomponent hydrodynamic scheme. In Fig. 10 we compare the kinetic and hydrodynamic solution for the 100-300 eV ramp problem early in the evolution (500 fs),

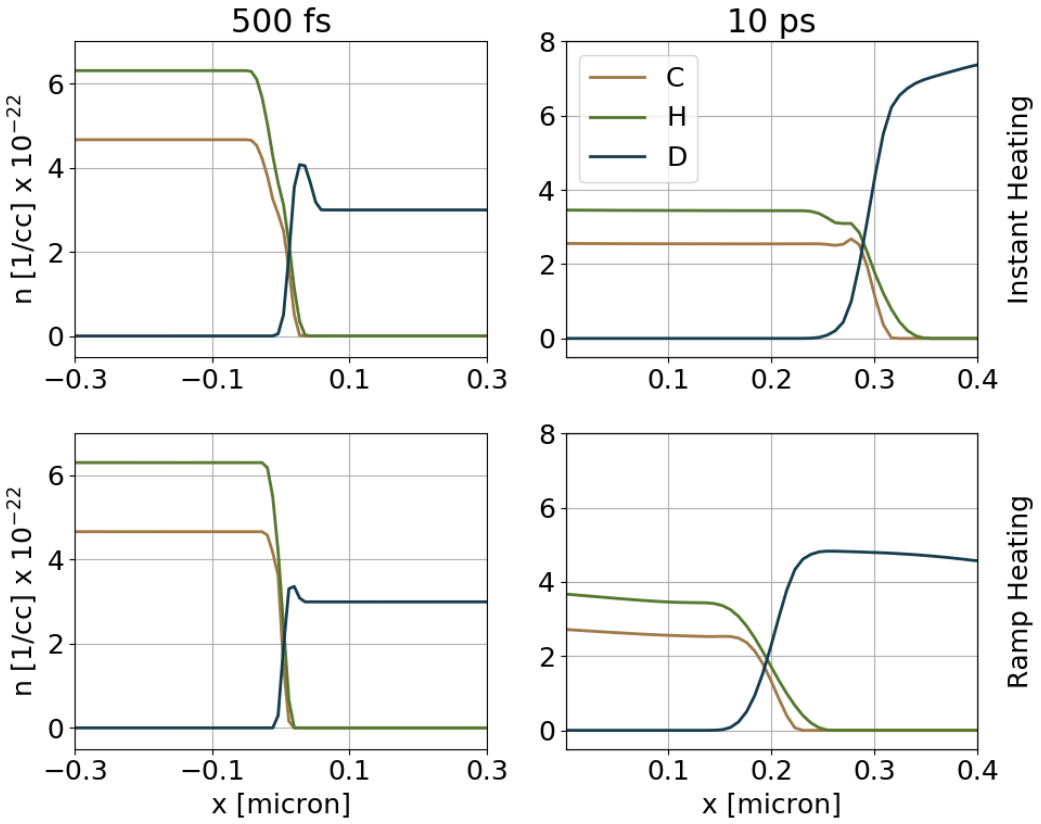

FIG. 4. **Density evolution for 10-50 eV interface test problem.** Number density plots are shown at 500 fs (first column) and 10 ps (second column). The instant heating case (first row) shows a separation between the hydrogen (brown, lightest line) and carbon (green, next darkest line) species, while this effect is somewhat less evident for the 10-50 eV temperature ramp case (second row). In the 500 fs plots, there is a compression of the deuterium species (blue, darkest line) as the interface moves into the gas portion of the domain. In the instant heating case at 10 ps, the simulation has run long enough that the data from the right side of the domain has reached the shell-gas interface due to the periodic boundary condition. The tritium and oxygen plots are excluded as there is very little tritium separation from the deuterium and the oxygen is a trace species.

when one would expect the kinetic effects to be strongest. We use 128 points in space and a velocity grid of 40^3, but now with a smaller spatial domain width of 10 microns. As before, the initial interface is at $x = 0$. The largest difference in the density profiles of the two solutions is well below one percent in this case, which suggests at the early stages of implosion a multicomponent hydrodynamics method that is consistent with this kinetic model is sufficient to model the dynamics.

To determine when kinetic effects begin to significantly affect the solution, we compare in Fig. 11 the kinetic and hydrodynamic number densities for the interface at 1 keV 20 keV. For the 1 keV case, we show the relative error between the kinetic and hydrodynamic solution at 5 ps. Within the mixing region, the errors remain reasonably small, but this appears to be a transition point where a kinetic description may begin to become necessary. At 20 keV, we see a clear difference in the solutions between the two methods due to the strong kinetic effects that are not captured in the hydrodynamic description.

E. Diffusion component comparisons

In the section, we present the relative sizes of the Fickean diffusion, barodiffusion, and electrodiffusion terms in the diffusion driving force (15). The formulas for these three components are expected to be valid when in the hydrodynamic limit. In Fig. 12 we show each component for the 100-300 eV case at 1 ps for shell hydrogen, shell carbon, and deuterium gas, respectively.

Recall that we use the PTF model for the Poisson term as it should have the greatest effect on the significance of the electrodiffusion term. In both the hydrogen and carbon shell materials, the Fickean diffusion term is most significant; however, there are nontrivial contributions from the barodiffusion and electrodiffusion. In particular for hydrogen, electrodiffusion is nearly as strong as the Fickean term. For the gas species at the interface, Fickean diffusion is the dominant contribution to the diffusive flux, while there is a slightly smaller but nontrivial contribution due to barodiffusion. However, the electrod-

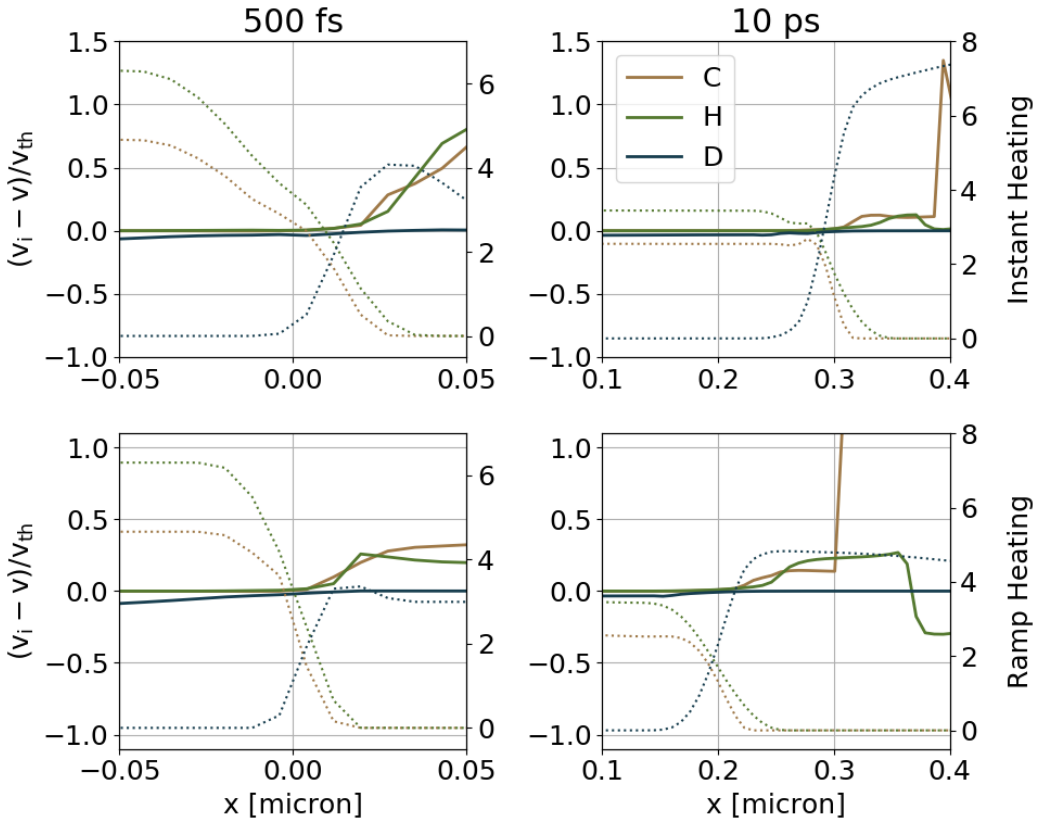

FIG. 5. **Diffusion velocity evolution for 10-50 eV interface test problem.** The normalized diffusion velocities $(\mathbf{v}_i - \mathbf{v}_0)/v_{th,i}$ are shown for hydrogen (brown, lightest line), carbon (green, next darkest line), and deuterium (blue, darkest line) at 500 fs (first column) and 10 ps (second column). For reference, the number densities are shown in the background as dashed lines. In both the instant heating (top row) and 10-50 eV ramp cases (second row), there are large deviations from the mixture velocity inside the mixing layer, which shows that the usual Chapman-Enskog transport theory does not apply.

iffusion and barodiffusion terms are much smaller than the Fickean term further into the gas material.

IV. CONCLUSION AND OUTLOOK

In summary, we have extended the multispecies, multitemperature BGK model from [25] to include additional multiphysics capabilities for more realistic simulations of dense plasma environments. The new model allows for higher-Z elements that can ionize/recombine during the dynamics, incorporates one-dimensional slab geometries with the inclusion of a Vlasov term, accounts for partially degenerate electrons through a modified Poisson equation, and uses collision rates derived from pre-computed screened Coulomb cross sections that are accurate for a wide range of plasma parameters.

Numerical results were obtained using a second-order finite volume method. When compared to recent studies using molecular dynamics [27], we are able to simulate over large domains, longer times, and at higher temperatures. However, unlike the MD simulations, the kinetic model has difficulty representing distribution functions with temperatures that span several orders of magnitude due to grid resolution constraints. Furthermore, the cryogenic temperatures at the start of the MD simulation are in a temperature and density regime for which kinetic theory is not appropriate. The changes to the initial condition to the kinetic model result in much faster initial ion speeds, which make direct comparison with MD results difficult. It should be pointed out that multispecies BGK operator does have an advantage over a multispecies Boltzmann operator, [48] because each species can have its own velocity grid. Species only interact with each other through moments, rather than the direct integration of distribution functions in the Boltzmann operator.

We applied the new model to a heated interface typical of the ablator-ice region in an ICF target at temperatures ranging from tens to thousands of eV. In all cases, there is a separation between the shell carbon and hydrogen species, with the lighter hydrogen jetting into the fuel region, possibly due to strong and persistent electric field effects. We also observed that there was diffusion

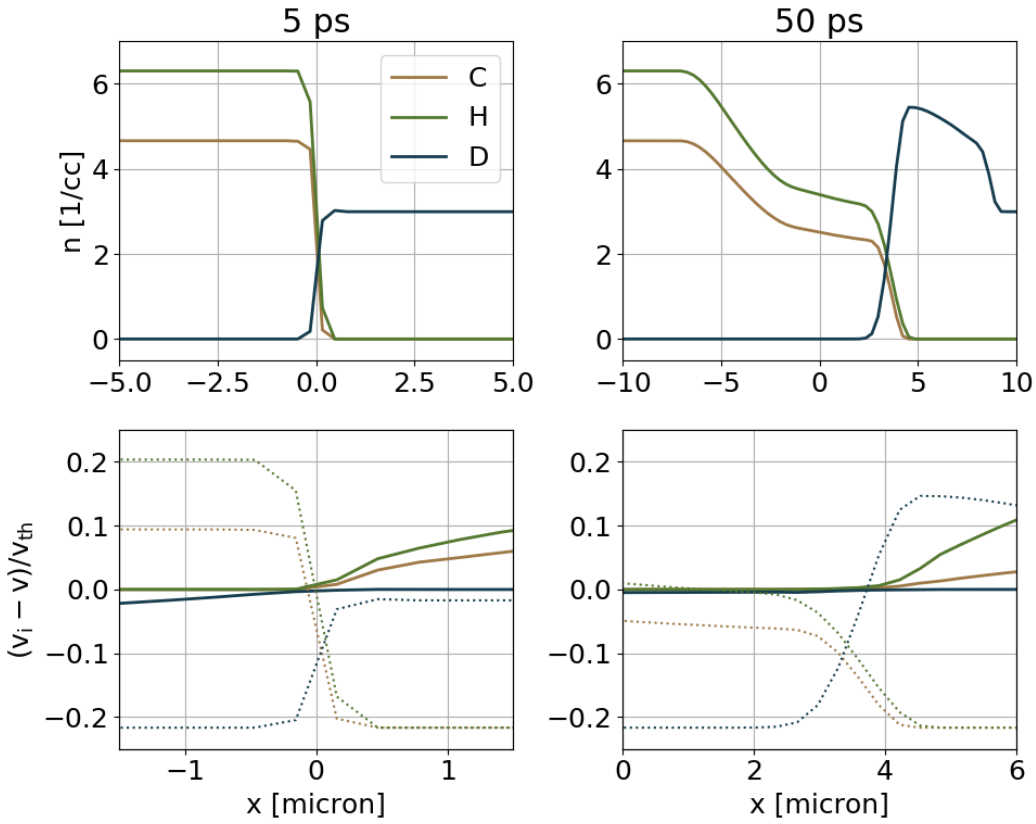

FIG. 6. **Density and diffusion velocity evolution for 100-300 eV interface test problem.** Number density (first row) and diffusion velocity $\mathbf{v}_i - \mathbf{v}_0$ (second row) plots are shown at 5 ps (first column) and 50 ps (second column). This simulation reaches time, length, and temperature scales that would be infeasible for a molecular dynamics calculation.

velocity separation in the mixing layer. Next, we examined kinetic effects during the mixing. A ratio of temperature components (parallel and perpendicular to the interface) was used as a metric for non-Maxwellian behavior; we found that for temperatures up to 1000 eV, the distribution functions in the mixing region remain close to Maxwellian with respect to the direction normal to the interface. These two observations imply that while the distribution function may be near equilibrium in the mixing region, a single velocity hydrodynamic model may not be enough to describe the dynamics. Morever, a multicomponent hydrodynamics model with a self-consistent electric field may be adequate for the early evolution of ICF capsule implosion. Kinetic effects only became significant at the very high temperatures expected later in the experiment, when the plasma is burning.

One key driver of the hydrogen jetting is the persistence of strong electric fields; we found that the nonlinear Poisson-Thomas-Fermi treatment, which takes electron degeneracy into account, predicts the strongest electric field effects. Linearizing the PTF model results in a weaker field that is qualitatively similar to the PB model. This similarity is likely due to the fact that both models tend to cause more screening than nonlinear, quantum-based models. For hydrogen, the diffusion component corresponding to the electric field was nearly as strong as the Fickean diffusion term.

The new physics capabilities in the extended BGK model, along with the reduced cost when compared to other kinetic models or MD simulations, make it an attractive choice to explore other phenomena in dense plasmas, including warm dense matter. Howover, the model can be improved and applied to other applications in many ways. For example, several natural extensions can be made to the multispecies BGK operator by simply following the developments found in the literature for the single species BGK model. One attractive feature of the single species model is that the collision term is easy to compute with an implicit solver [49]. Generalization of this procedure to the multispecies case would obviate the need to resolve the often restrictive collision time scale, especially for collisions with electrons. Another extension is to include additional degrees of freedom in the target Maxwellians in (9) as is done in the ES-BGK model [33]. We also plan to investigate methods that alleviate the grid resolution problem mentioned in Sec. III and thereby enable the representation of distributions of very different temperatures. The results presented in

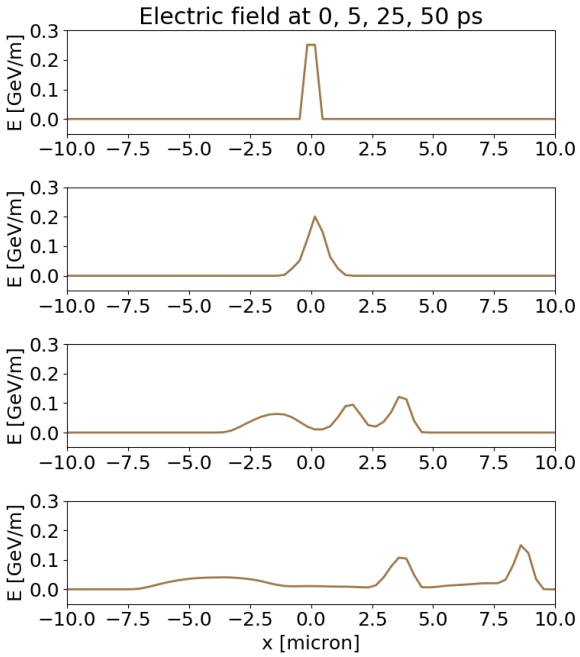

FIG. 7. **Electric field for 100-300 eV interface test problem.** The self-consistent electric field is shown at four times: 0 fs, 5 ps, 25 ps, 50 ps. The electric field persists at a similar order of magnitude for the entire simulation.

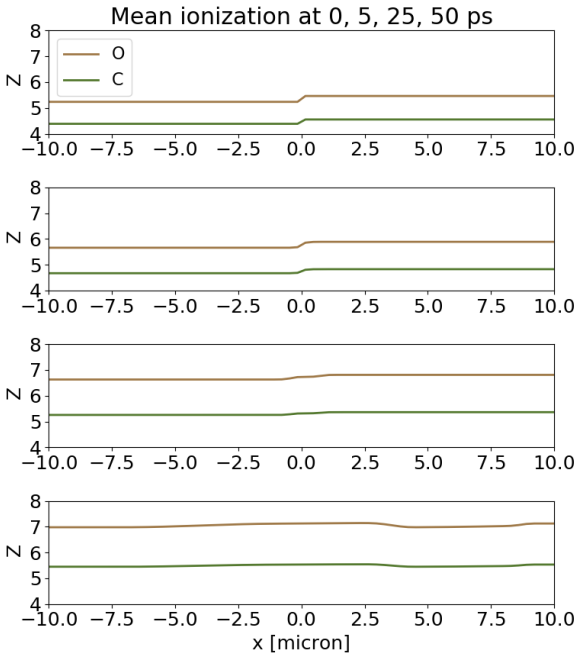

FIG. 8. **Ionization states for 100-300 eV interface test problem.** The ionization states of carbon (lower green line) and oxygen (upper brown line) are shown at four times: 0 fs, 5 ps, 25 ps, 50 ps. The multispecies kinetic model dynamically updates the ionization state, which affects both the electric fields and the collision rates. The hydrogenic species ionization states are all near unity in this density and temperature range, so they are excluded from this plot.

this paper should be corroborated with another code or model, such as a Boltzmann or Fokker-Planck equation consistent with these plasma conditions, as the higher temperature test cases are beyond the range that MD can simulate. Future work will also seek to model electrons explicitly as one of the dynamical species; we will seek to build effective potential collision rates [26] that also include quantum effects to correctly model the electron interactions. Such a model would include additional plasma properties, such as electronic thermal conductivity, in a self-consistent way and thus enable a wider range of possible applications.

Finally, another possible addition to this model is the inclusion of magnetic fields. This is a non-trivial addition, as it would both require solution of Maxwell's equations rather than the relatively simpler Poisson equation as well as recomputing the transport coefficients and adding the tensor character and additional dimensions required to the code. Furthermore, for many of the systems for which it is appropriate to use a BGK description, the gyrofrequency time scale is much longer than the collision time scale, so these effects may be less important. For the ICF inspired experiment considered in this paper, the magnetic fields would need to be on the order of a gigaGauss for the gyrofrequency to be of similar order as the collision frequency. Furthermore, the presence of collisions may suppress the growth of self-generated magnetic fields for this problem [50, 51], though it is possible that fields of this strength may arise in ICF experiments [52]. For other applications such as magnetic confinement fusion where the fuel number densities are much smaller, or astrophysical applications, inclusion of magnetic fields will obviously become more important and will be the subject of future work.

Acknowledgements

We would like to thank Jim Glosli and Liam Stanton, both of Lawrence Livermore National Laboratory, for sharing MD results as well as the MD implementation of the mean ionization state for mixtures. This manuscript has been authored, in part, by UT-Battelle, LLC, under Contract No. DE-AC0500OR22725 with the U.S. Department of Energy. The United States Government retains and the publisher, by accepting the article for publication, acknowledges that the United States Government retains a non-exclusive, paid-up, irrevocable, world-wide license to publish or reproduce the published form of this manuscript, or allow others to do so, for the United States Government purposes. The Department of Energy will provide public access to these results of federally sponsored research in accordance with the DOE Public Access Plan (http://energy.gov/downloads/doe-public-access-plan). The research of CH was sponsored by the Office of Advanced Scientific Computing Research and performed at the Oak Ridge National Laboratory,

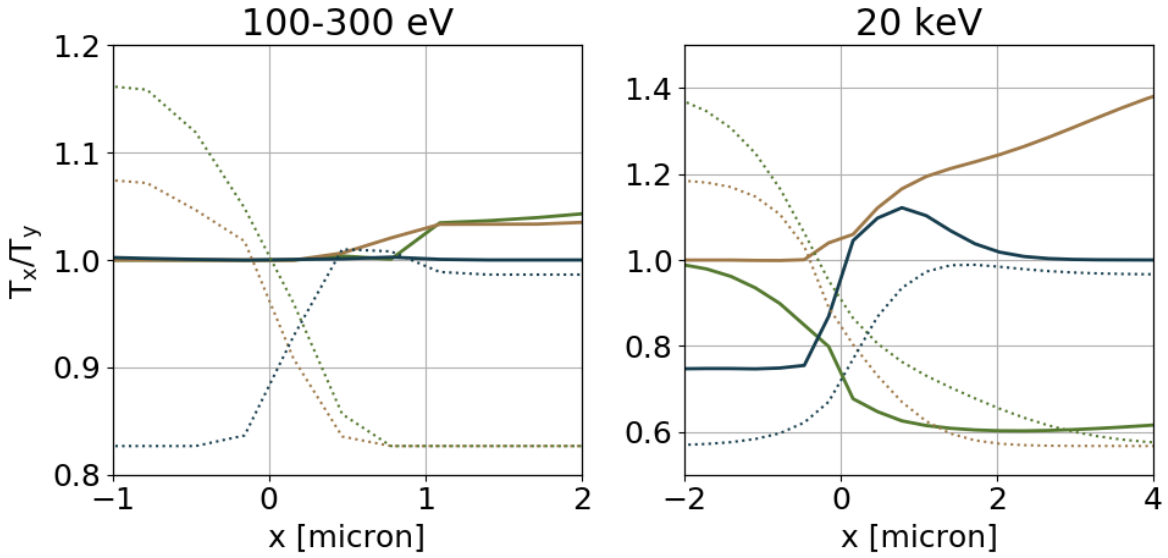

FIG. 9. **Temperature component ratio for 100-300 eV and 20 kEV case.** Ratios of the normal and transverse temperature components for the 100-300 eV ramp test case and 20 keV test case is shown for H (brown, lightest line), C (green, next darkest line), and D (blue, darkest line) at 5 ps and 0.5 ps, respectively. For reference, the number densities are plotted as dashed lines in the background. This suggests that in the low temperature case, the distributions remain close to Maxwellian in the mixing layer.

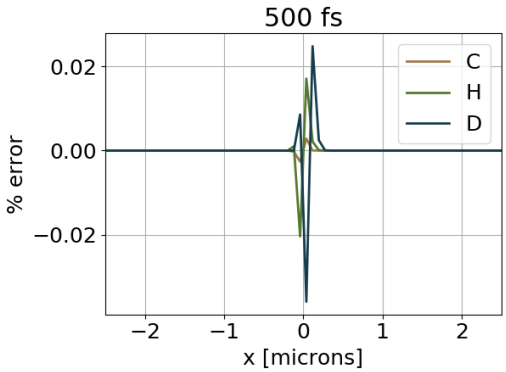

FIG. 10. **Comparison of kinetic and hydrodynamic number densities for the 100-300eV case.** The relative difference of the number densities between the kinetic solution and a multivelocity hydrodynamic solution is shown for the 100-300 eV ramp test case. The relative difference in number density for H (brown, lightest line), C (green, next darkest line), and D (blue, darkest line) is shown at 500 fs. At these low temperatures, a multivelocity hydrodynamics code may be enough to accurately capture the dynamics.

which is managed by UT-Battelle, LLC under Contract No. DE-AC0500OR22725. The research of JH and MSM was performed as part of the NAMBE Project under the auspices of the U.S. Department of Energy by Los Alamos National Laboratory under Contract DE-AC52-06NA25396. Los Alamos Report LA-UR-17-25906.

[1] R. Betti and O. A. Hurricane, Nature Phys. **12**, 435 (2016).
[2] O. A. Hurricane, D. A. Callahan, D. T. Casey, P. M. Celliers, C. Cerjan, E. L. Dewald, T. R. Dittrich, T. Doppner, D. E. Hinkel, L. F. B. Hopkins, J. L. Kline, S. Le Pape, T. Ma, A. G. MacPhee, J. L. Milovich, A. Pak, H. S. Park, P. K. Patel, B. A. Remington, J. D. Salmonson, P. T. Springer, and R. Tommasini, Nature

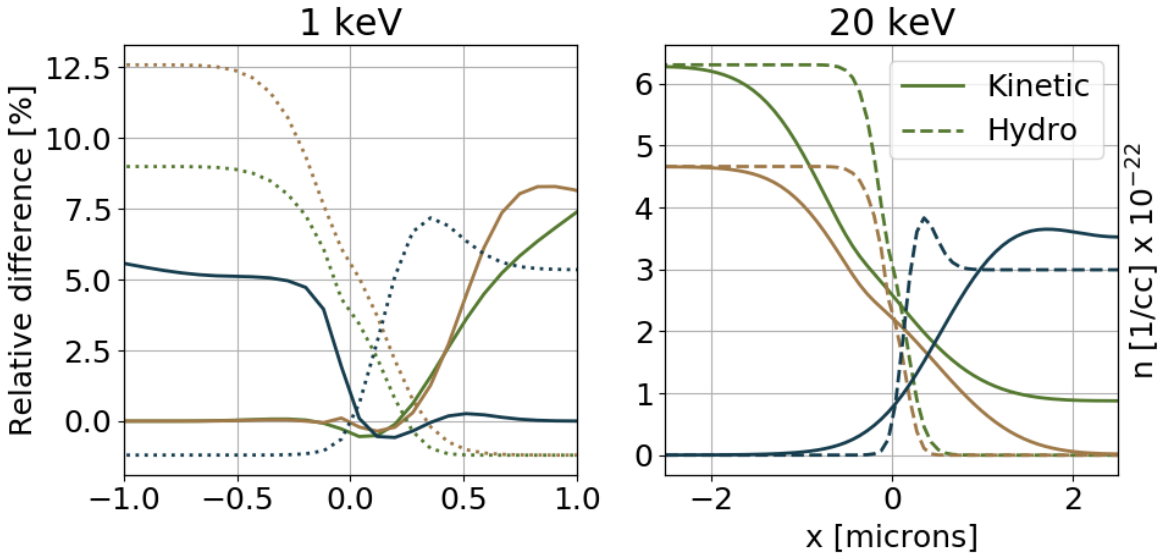

FIG. 11. **Comparison of kinetic and hydrodynamic number densities for the 1 keV and 20 keV case.** In the left plot, we show the relative error in the number density between the kinetic and hydrodynamic models at 1 keV and 5 ps. This appears to be a transition point where a multicomponent hydrodynamic model would begin to break down for this problem. In the right plot, we show the number densities from the kinetic (solid lines) and hydrodynamic (dashed lines) models. At this high temperature, the kinetic effects are strong and the hydrodynamic description no longer applies.

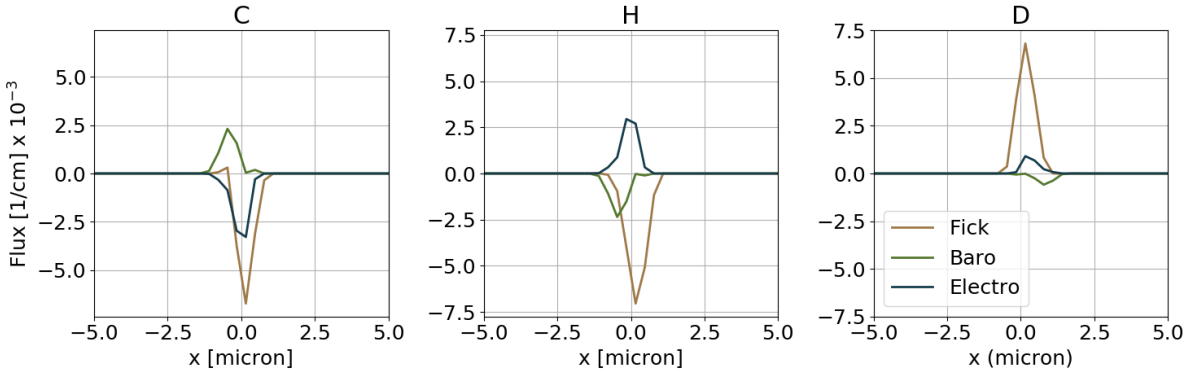

FIG. 12. **Diffusion components for 100-300 eV test problem.** The Fickean (brown, lightest line), Barodiffusion (green, next darkest line), and Electrodiffusion (blue, darkest line) contributions to the carbon (left), hydrogen (center), and deuterium (right) diffusive fluxes are shown at 5 ps for the 100-300 eV ramp test case. All three types of diffusion appear to have a significant effect on the mass flux.

506, 343 (2014).
[3] V. A. Smalyuk, S. Hu, J. Hager, J. Deletterez, D. Meyerhofer, T. Sangster, and D. Shvarts, Phys. Rev. Lett. **103**, 105001 (2009).
[4] H. G. Rinderknecht, H. Sio, C. K. Li, A. B. Zylstra, M. J. Rosenberg, P. Amendt, J. Delettrez, C. Bellei, J. A. Frenje, M. Gatu Johnson, F. H. Séguin, R. D. Petrasso, R. Betti, V. Y. Glebov, D. D. Meyerhofer, T. C. Sangster, C. Stoeckl, O. Landen, V. A. Smalyuk, S. Wilks, A. Greenwood, and A. Nikroo, Phys. Rev. Lett. **112**, 135001 (2014).
[5] J. R. Rygg, J. A. Frenje, C. K. Li, F. H. Sguin, R. D. Petrasso, J. A. Delettrez, V. Y. Glebov, V. N. Goncharov, D. D. Meyerhofer, S. P. Regan, T. C. Sangster, and C. Stoeckl, Physics of Plasmas **13**, 052702 (2006), http://dx.doi.org/10.1063/1.2192759.
[6] H. W. Herrmann, J. R. Langenbrunner, J. M. Mack, J. H. Cooley, D. C. Wilson, S. C. Evans, T. J. Sedillo, G. A. Kyrala, S. E. Caldwell, C. S. Young, A. Nobile, J. Wermer, S. Paglieri, A. M. McEvoy, Y. Kim, S. H. Batha, C. J. Horsfield, D. Drew, W. Garbett, M. Rubery, V. Y. Glebov, S. Roberts, and J. A. Frenje, Physics of Plasmas **16**, 056312 (2009), http://dx.doi.org/10.1063/1.3141062.
[7] P. Amendt, O. L. Landen, H. F. Robey, C. K. Li, and

R. D. Petrasso, Phys. Rev. Lett. **105**, 115005 (2010).
[8] P. Amendt, S. C. Wilks, C. Bellei, C. K. Li, and R. D. Petrasso, Phys. Plasmas **18**, 056308 (2011).
[9] L. Yin, B. J. Albright, W. Taitano, E. L. Vold, L. Chacón, and A. N. Simakov, Phys. Plasmas **23**, 112302 (2016).
[10] W. Bang, B. J. Albright, P. A. Bradley, E. L. Vold, J. C. Boettger, and J. C. Fernández, Scientific Reports **6**, 29441 (2016).
[11] C. K. Li, F. H. Séguin, J. R. Rygg, J. A. Frenje, M. Manuel, R. D. Petrasso, R. Betti, J. Delettrez, J. P. Knauer, F. Marshall, D. D. Meyerhofer, D. Shvarts, V. A. Smalyuk, C. Stoeckl, O. L. Landen, R. P. J. Town, C. A. Back, and J. D. Kilkenny, Phys. Rev. Lett. **100**, 225001 (2008).
[12] A. Bannerjee, R. A. Gore, and M. J. Andrews, Phys. Rev. E , 046309 (2010).
[13] M. Gittings, R. Weaver, M. Clover, T. Betlach, N. Byrne, R. Coker, E. Dendy, R. Hueckstaedt, K. New, W. R. Oakes, D. Ranta, and R. Stefan, Computational Science & Discovery **1**, 015005 (2008).
[14] J. Waltz and T. A. Gianakon, Comp. Phys. Comm. **183**, 70 (2012).
[15] M. Marinak, G. Kerbel, N. Gentile, O. Jones, D. Munro, S. Pollaine, T. Dittrich, and S. Haan, Phys. Plasmas **8**, 2275 (2001).
[16] N. M. Hoffman, G. B. Zimmerman, K. Molvig, H. G. Rinderknecht, M. J. Rosenberg, B. J. Albright, A. N. Simakov, H. Sio, A. B. Zylstra, M. G. Johnson, F. H. Sguin, J. A. Frenje, C. K. Li, R. D. Petrasso, D. M. Higdon, G. Srinivasan, V. Y. Glebov, C. Stoeckl, W. Seka, and T. C. Sangster, Physics of Plasmas **22**, 052707 (2015).
[17] A. N. Simakov and K. Molvig, Physics of Plasmas **23**, 032115 (2016).
[18] A. N. Simakov and K. Molvig, Physics of Plasmas **23**, 032116 (2016).
[19] S. Atzeni, A. Schiavi, F. Califano, F. Cattani, F. Cornolti, D. Del Sarto, T. Liseykina, A. MacChi, and F. Pegoraro, Computer Physics Communications **169**, 153 (2005).
[20] C. Bellei, H. Rinderknecht, A. Zylstra, M. Rosenberg, H. Sio, C. K. Li, R. Petrasso, S. C. Wilks, and P. A. Amendt, Physics of Plasmas **21**, 056310 (2014).
[21] B. E. Peigney, O. Larroche, and V. Tikhonchuk, Physics of Plasmas **21**, 122709 (2014).
[22] W. T. Taitano, L. Chacón, A. N. Simakov, and K. Molvig, J. Comput. Phys. **297**, 357 (2015).
[23] T. Haxhimali, R. E. Rudd, W. H. Cabot, and F. R. Graziani, Phys. Rev. E **92**, 053110 (2015).
[24] T. Haxhimali, R. E. Rudd, W. H. Cabot, and F. R. Graziani, Phys. Rev. E **90**, 023104 (2014).
[25] J. R. Haack, C. D. Hauck, and M. S. Murillo, J. Stat. Phys. **168**, 822 (2017).
[26] L. G. Stanton and M. S. Murillo, Phys. Rev. E **93**, 043203 (2016).
[27] L. G. Stanton, J. N. Glosli, and M. S. Murillo, Phys. Rev. X (2017), submitted.
[28] "Dense plasma properties database," `https://github.com/MurilloGroupMSU/Dense-Plasma-Properties-Database` (2017).
[29] L. D. Landau, Zh. eks. teor. phys. **7**, 203 (1937).
[30] S. Chapman and C. Cowling, *The Mathematical Theory of Non-Uniform Gases* (Cambridge University Press, Cambridge, 1970).
[31] The function $\mathcal{K}_{11}$ is the nondimensional version of the so-called collision integral $\Omega^{(11)}$ used in [30] to define transport coefficients and corresponds to an integration against the Boltzmann momentum transfer cross section.
[32] J. P. Hansen, F. Joly, and J. R. McDonald, Physica A **132**, 472 (1985).
[33] H. Holway, Phys. Fluids **9**, 1658 (1966).
[34] R. M. More, Adv. At. Mol. Phys. **21**, 305 (1985).
[35] M. S. Murillo, J. Weisheit, S. B. Hansen, and M. W. C. Dharma-Wardana, Phys. Rev. E **87**, 0613113 (2013).
[36] F. Graziani *et al.*, High Energy Density Physics **8**, 105 (2012).
[37] S. Ichimaru, H. Iyetomi, and S. Tanaka, Physics Reports **149**, 91 (1987).
[38] F. R. Graziani, J. D. Bauer, and M. S. Murillo, Phys. Rev. E **90**, 033104 (2014).
[39] This is different from the Boltzmann-Poisson equation used in e.g., modeling semiconductors, which dynamically evolves electrons and assumes a fixed ion charge distribution when determining the electric field.
[40] Many scientific computing libraries contain implementations for accurate and efficient evaluation of this integral; we use the GNU Scientific Library [53] in this paper.
[41] R. Levque, *Finite Volume Methods for Hyperbolic Problems* (Cambridge University Press, Cambridge, 2002).
[42] S. Gottlieb, J. Sci. Comput. , 105 (2005).
[43] L. Mieussens and S. Brull, J. Comput. Phys. **266**, 22 (2014).
[44] S. Brull, L. Mieussens, and L. Forestier-Coste, in *Proceedings of the 30th International Symposium on Rarefied Gas Dynamics* (2016) p. 180002.
[45] W. T. Taitano, L. Chacón, and A. N. Simakov, J. Comput. Phys. **318**, 391 (2016).
[46] For these one dimensional problems, the distribution function properties are identical in the transverse directions y and z.
[47] K. Xu and K. H. Prendergast, J. Comput. Phys. **114**, 9 (1994).
[48] A. Munafo, J. Haack, I. M. Gamba, and T. Magin, J. Comput. Phys. **264**, 152 (2014).
[49] F. Coron and B. Perthame, SIAM J. Num. Anal. **28**, 26 (1991).
[50] E. S. Weibel, Phys. Rev. Lett. **2**, 83 (1958).
[51] D. D. Ryutov, F. Fiuza, C. M. Huntington, J. S. Ross, and H.-S. Park, Phys. Plasmas **21**, 032701 (2014).
[52] R. J. Kingham and A. R. Bell, Phys. Rev. Lett. **88**, 045004 (2002).
[53] "GNU scientific library," `http://www.gnu.org/software/gsl/` (2017).